# Coherency Matrix Decomposition Based Polarimetric Persistent Scatterer Interferometry

Feng Zhao, *Student Member, IEEE*, and Jordi J. Mallorqui, *Senior Member, IEEE*

*Abstract*—The rationale of polarimetric optimization techniques is to enhance the phase quality of the interferograms by combining adequately the different polarization channels available to produce an improved one. Different approaches have been proposed for Polarimetric Persistent Scatterer Interferometry (PolPSI). They range from the simple and computationally efficient BEST, where for each pixel the polarimetric channel with the best response in terms of phase quality is selected, to those with high computational burden like the Equal Scattering Mechanism (ESM) and the Sub-Optimum Scattering Mechanism (SOM). BEST is fast and simple but it does not fully exploit the potentials of polarimetry. On the other side, ESM explores all the space of solutions and finds the optimal one but with a very high computational burden. A new PolPSI algorithm, named CMD-PolPSI, is proposed to achieve a compromise between phase optimization and computational cost. Its core idea is utilizing the PolSAR coherency matrix decomposition to determine the optimal polarization channel for each pixel. Three different PolSAR image sets of both full- (Barcelona) and dual-polarization (Murcia and Mexico City) have been used to evaluate the performance of CMD-PolPSI. The results show that CMD-PolPSI presents better optimization results than BEST method by using either $D_A$ or temporal mean coherence as phase quality metrics. Compared with the ESM algorithm, CMD-PolPSI is 255 times faster but its performance is not as optimal. The influence of the number of available polarization channels and pixel's resolutions on the CMD-PolPSI performance is also discussed.

*Index Terms*—Polarimetric Persistent Scatterer Interferometry (PolPSI), ground deformation monitoring, interferometric phase optimization, pixel density, Mexico City.

## I. INTRODUCTION

**P**ERSISTENT Scatterer Interferometry (PSI), which is based on Differential SAR Interferometry (DInSAR), has been proposed and developed in the last two decades [1]–[9]. This remote sensing technique is efficient and able to retrieve ground movement with millimetric precision [10], [11], which make it a routinely used tool for ground deformation monitoring. To reduce the effect of the noise induced by different decorrelation sources, PSI only exploits SAR pixels that preserve their phase qualities along time. Therefore, pixel selection is a mandatory step in all PSI techniques, and PSI

Feng Zhao and J. J. Mallorqui are with the CommSensLab, Universitat Politècnica de Catalunya, 08034 Barcelona, Spain (e-mail: feng.zhao@tsc.upc.edu; mallorqui@tsc.upc.edu).

techniques' characteristics are determined to a large extend by the kind of targets they are utilizing.

According to the types of exploring targets, classical PSI techniques can be in general classified into two categories. The first category exploits deterministic or permanent scatterers (PSs), which usually correspond to man-made structures or rocky areas. These point-like scatterers are time-invariant and spatially concentrated, thus they are slightly impacted by spatial or temporal decorrelation. The classical PSI technique of this first category is the so-called PSInSAR technique, which identifies PSs by using their dispersion of amplitude ($D_A$) [1]. There are also some other phase quality metrics for PSs' identification, such as the TPC (temporal phase coherence) [6], [12] and TSC (temporal sublook coherence) [9], which define other two PSI approaches of this category.

The other category of PSI is based on the coherence stability, which works over multilooked interferograms, and the SBAS and CPT algorithms [3], [4], [8] are of this category. This kind of PSI techniques are able to work on both deterministic scatterers and distributed scatterers (DSs). However, the multilook employed in this category of PSI reduces SAR images' resolutions and, as a consequence, details can be lost in heterogeneous areas.

More advanced PSI techniques, like SqueeSAR [13] and CAESAR [14], which can jointly adaptive process both PSs and DSs have been proposed. SqueeSAR and its variants are based on adaptive filters, which are constructed by similarity tests between pixels, to classify and adaptive filter PSs and DSs. CAESAR, inspired by PolSAR decomposition techniques, tries to separate different scattering mechanisms within one pixel by analyzing the pixel's covariance matrix. Thus, it has the ability to reduce decorrelation noise of DSs and mitigate the layover effects in urban areas for PSs [14].

Mainly due to the shortage of long time-series polarimetric SAR (PolSAR) data, PSI techniques had been traditionally limited to a single polarimetric channel. As more SAR satellites with polarimetric capabilities have been launched, it is feasible to extend PSI to the polarimetric case. Therefore, the Polarimetric PSI (i.e. PolPSI) was introduced [15] and has been developed to improve deformation detection and characterization by increasing the density and quality of valid pixels w.r.t. the single-polarimetric case. Starting from the so-called BEST method [15], which selects the polarimetric channel with the highest quality estimator among all available channels, PolPSI techniques have been evolved to more advanced algorithms that search the optimal polarimetric channel in more extended spaces like the Equal Scattering Mechanism (ESM) and Sub-Optimum Scattering Mechanism (SOM) [16]–

[21]. Moreover, besides the classical $D_A$ and coherence metrics, other phase quality estimators like the TSC [22] and TPC [23] have also been employed in phase optimization of PolPSI to improve its performance. Meanwhile, as PSs and DSs appear simultaneously in real scenarios, a PolPSI technique inspired by SqueeSAR [13] was proposed by Navarro-Sanchez to adaptive optimize these two kinds of scatterers [24].

The above-mentioned PolPSI techniques, except the classical BEST, search for an optimal polarimetric channel in a defined solution space for every pixel, which is very time-consuming and may limit their applications in practice for large scenes. For instance, ESM explores the full space of solutions to find the optimal one. Other efficient methods [25], [26] have been investigated to reduce the computational time of polarimetric coherence optimization. Unfortunately, they can hardly be applied on polarimetric optimizations based on full-resolution quality metrics, like $D_A$. On the other side, the BEST method, which simply selects the best channel among all available, is not able to fully exploit the information of PolSAR images but its computational burden is extremely low.

In this paper, a new PolPSI approach with a good compromise between computation burden and phase optimization performance is proposed. This approach has been named as CMD-PolPSI and it uses the coherency matrix decomposition to determine the optimal polarimetric channel. It does not have to search for the solution within the full space of solutions and the optimization, despite it is not as optimal than with ESM, outperforms BEST. To assess the performance of the proposed CMD-PolPSI, it has been tested with three different PolSAR data sets. One is the quad-pol Radarsat-2 images acquired over Barcelona (Spain), the other two are dual-pol TerraSAR-X and Sentinel-1B data sets acquired over Murcia (Spain) and Mexico City (Mexico), respectively. All the three test sites are affected by subsidence phenomena. The benefits of the proposed CMD-PolPSI regarding phase quality improvement and pixel densities of the final deformation maps have been evaluated and discussed.

The paper is organized as follows. Section II describes the detailed procedures of the proposed PolPSI algorithm. In Section III, data sets of the three test sites are briefly introduced. Then, the phase quality optimization and deformation estimation results obtained with the proposed and traditional methods are compared in Section IV. In Section V, some aspects influencing the performance of CMD-PolPSI are discussed. Finally, conclusions are made in Section VI.

## II. METHODS

### A. Vector Interferometry

Polarimetric SAR interferometry (PolInSAR) is based on two polarimetric SAR images acquired from two spatially separated locations [20], [27]. In monostatic systems the assumption of reciprocity can be applied and for quad-pol SAR data sets the PolSAR scattering vector $\boldsymbol{k}$ under Pauli basis can be obtained with

$$\boldsymbol{k} = \frac{1}{\sqrt{2}}[S_{hh} + S_{vv},\ S_{hh} - S_{vv},\ 2S_{hv}]^T \quad (1)$$

where $T$ means the transpose, $S_{hh}$ and $S_{vv}$ stand for the horizontal and vertical co-polar channels, respectively, and $S_{hv}$, equal to $S_{vh}$ in the monostatic case, is the cross-polar channel of the scattering matrix [28]. If the data is dual-pol, (1) is replaced by (2) if only the co-polar channels are available,

$$\boldsymbol{k} = \frac{1}{\sqrt{2}}[S_{hh} + S_{vv},\ S_{hh} - S_{vv}]^T \quad (2)$$

or by (3) if a co-polar $xx$ and the cross-polar channels are available,

$$\boldsymbol{k} = [S_{xx},\ 2S_{hv}]^T. \quad (3)$$

Then the PolInSAR vector can be defined as

$$\boldsymbol{K} = [\boldsymbol{k}_1,\ \boldsymbol{k}_2]^T \quad (4)$$

where $\boldsymbol{k}_1$ and $\boldsymbol{k}_2$ are the two scattering vectors from the master and slave PolSAR images that form the interferogram. To generate a single interferogram based on $\boldsymbol{K}$, two normalized complex projection vectors $\boldsymbol{\omega}_1$ and $\boldsymbol{\omega}_2$ are introduced [27], [28]. These two vectors can be interpreted as two scattering mechanisms (SMs), and the two PolInSAR vectors $\boldsymbol{k}_1$ and $\boldsymbol{k}_2$ can be projected onto them, respectively

$$\mu_i = \boldsymbol{\omega}_i^\dagger \cdot \boldsymbol{k}_i,\ \ i = 1, 2 \quad (5)$$

where $\dagger$ refers to the conjugate transpose, $\mu_1$ and $\mu_2$ are the two scattering coefficients, analogous to single-polarization SAR images [27], [28]. To avoid introducing artificial changes in the phase centers of the scatterers in PolPSI applications, $\boldsymbol{\omega}_1$ and $\boldsymbol{\omega}_2$ are forced to be identical to one optimal projection vector $\boldsymbol{\omega}$ for all the interferograms [21], [27], [29].

*1) Deterministic Scatterers (PSs):* For deterministic scatterers, $\boldsymbol{k}_i$ in (5) corresponds to a deterministic vector [21], [24], [28]. The expression for vector interferogram can be obtained as [27]

$$Intf = \mu_1 \cdot \mu_2^* \quad (6)$$

where $*$ is the complex conjugate. The commonly used pixel phase quality criterion for PSs is the amplitude dispersion $D_A$, which can be can be expressed as [16], [21]

$$D_A = \frac{\sigma_A}{m_A} = \frac{1}{|\boldsymbol{\omega}^\dagger \boldsymbol{k}|} \sqrt{\frac{1}{N} \sum_{i=1}^{N} \left( |\boldsymbol{\omega}^\dagger \boldsymbol{k}_i| - \overline{|\boldsymbol{\omega}^\dagger \boldsymbol{k}|} \right)^2} \quad (7)$$

with

$$\overline{|\boldsymbol{\omega}^\dagger \boldsymbol{k}|} = \frac{1}{N} \sum_{i=1}^{N} |\boldsymbol{\omega}^\dagger \boldsymbol{k}_i| \quad (8)$$

where $\sigma_A$ and $m_A$ are the standard deviation and mean of the images' amplitudes, $N$ is the number of images and the over line indicates the empirical mean value [16], [21].

*2) Distributed Scatterers (DSs):* For distributed scatterers, (4) behaves as a random vector due to the complex stochastic scattering process within one resolution cell [21], [24]. In this case, the $6 \times 6$ (for full-pol data) or $4 \times 4$ (for dual-pol data) PolInSAR coherency matrix $\boldsymbol{T}_6$ or $\boldsymbol{T}_4$ are defined as (9) to characterize the scatterers' behaviors

$$\boldsymbol{T}_6 \setminus \boldsymbol{T}_4 = E\{\boldsymbol{k}\boldsymbol{k}^\dagger\} = \begin{bmatrix} \boldsymbol{T}_{11} & \boldsymbol{\Omega}_{12} \\ \boldsymbol{\Omega}_{12}^\dagger & \boldsymbol{T}_{22} \end{bmatrix} \quad (9)$$

where $E$ is the expectation operator, which is usually implemented with a spatial neighboring average [27], [28]. $\boldsymbol{T}_{11}$ and $\boldsymbol{T}_{22}$ are the individual coherency matrices and $\boldsymbol{\Omega}_{12}$ is the PolInSAR coherency matrix given by [27]

$$\boldsymbol{T}_{11} = E\{\boldsymbol{k}_1\boldsymbol{k}_1^\dagger\} \quad \boldsymbol{T}_{22} = E\{\boldsymbol{k}_2\boldsymbol{k}_2^\dagger\} \quad \boldsymbol{\Omega}_{12} = E\{\boldsymbol{k}_1\boldsymbol{k}_2^\dagger\}. \tag{10}$$

Then the vector interferogram can be obtained with

$$Intf = E\{\mu_1 \cdot \mu_2^*\} = E\{(\boldsymbol{\omega}^\dagger\boldsymbol{k}_1)(\boldsymbol{\omega}^\dagger\boldsymbol{k}_2)^\dagger\} \\ = \boldsymbol{\omega}^\dagger E\{\boldsymbol{k}_1\boldsymbol{k}_2^\dagger\}\boldsymbol{\omega} = \boldsymbol{\omega}^\dagger\boldsymbol{\Omega}_{12}\boldsymbol{\omega} \tag{11}$$

from which the interferometric phase can be derived as $arg(\boldsymbol{\omega}^\dagger\boldsymbol{\Omega}_{12}\boldsymbol{\omega})$. The corresponding coherence $\gamma(\boldsymbol{\omega})$ is then given by [27], [28]

$$\gamma(\boldsymbol{\omega}) = \frac{|\boldsymbol{\omega}^\dagger\boldsymbol{\Omega}_{12}\boldsymbol{\omega}|}{\sqrt{\boldsymbol{\omega}^\dagger\boldsymbol{T}_{11}\boldsymbol{\omega}}\sqrt{\boldsymbol{\omega}^\dagger\boldsymbol{T}_{22}\boldsymbol{\omega}}}. \tag{12}$$

For PolPSI applications, the mean coherence $\overline{\gamma}$ expressed by (13) is used as the interferometric phase quality estimation [16], [21], [24]

$$\overline{\gamma} = \frac{1}{N_{intf}} \sum_{k=1}^{N_{intf}} \gamma(\boldsymbol{\omega})_k \tag{13}$$

where $N_{intf}$ is the number of interferograms.

It can be seen from (7) and (13) that the two phase quality estimators $D_A$ and $\overline{\gamma}$ are both influenced by the projection vector $\boldsymbol{\omega}$. Therefore, phase optimization in PolPSI consists in searching for the optimal projection vector $\boldsymbol{\omega}$ that minimizes $D_A$ or maximizes $\overline{\gamma}$. The simple BEST method simply selects the polarization channel with the highest estimated phase quality. The ESM approach explores the full space of solutions while SOM just a subspace, both at the price of a high computational burden. The detailed implementation of the three methods can be found in [21].

### B. Eigenvector-Based Coherency Matrix Decomposition

To reduce the effects of speckle noise, spatially or temporally averaged coherency matrices may be used for eigenvector-based decomposition [28]. Since spatial averaging degrades images' resolution, the time-series mean coherency matrix $\overline{\boldsymbol{T}}$ is used for the decomposition to preserve resolution. This time-series mean coherency matrix $\overline{\boldsymbol{T}}$ can be calculated by

$$\overline{\boldsymbol{T}} = \frac{1}{N} \sum_{i=1}^{N} \boldsymbol{k}_i \cdot \boldsymbol{k}_i^\dagger \tag{14}$$

where $N$ is the number of acquisitions and $\boldsymbol{k}_i$ the scattering vector of the $i$th acquisition given by equations (1)-(3).

Once $\overline{\boldsymbol{T}}$ has been obtained, for a full-resolution analysis (for deterministic scatterers, $D_A$ based optimization), the eigenvector-based decomposition is applied directly on $\overline{\boldsymbol{T}}$. For distributed scatterers' analysis (mean coherence $\overline{\gamma}$ based optimization), $\overline{\boldsymbol{T}}$ is spatially averaged before the decomposition. Then the temporal or temporal-spatial mean coherency matrix $\overline{\boldsymbol{T}}$ can be decomposed into

$$\overline{\boldsymbol{T}} = \sum_{i=1}^{q} \lambda_i \cdot \boldsymbol{u}_i \cdot \boldsymbol{u}_i^\dagger \tag{15}$$

where $q$ is the number of polarimetric channels and $\lambda_i$ and $\boldsymbol{u}_i$ are respectively the eigenvalue and corresponding eigenvector of $\overline{\boldsymbol{T}}$ [27], [28].

When full-pol SAR data is available ($q = 3$), there are three eigenvalues with $\lambda_1 \geq \lambda_2 \geq \lambda_3 \geq 0$, and their three corresponding eigenvectors $\boldsymbol{u}_1$, $\boldsymbol{u}_2$ and $\boldsymbol{u}_3$. For the dual-pol case ($q = 2$), there are two eigenvalues with $\lambda_1 \geq \lambda_2 \geq 0$, and their associated eigenvectors $\boldsymbol{u}_1$ and $\boldsymbol{u}_2$. These eigenvectors are unitary complex vectors and orthogonal to each other. Moreover, these eigenvectors represent different scattering mechanisms (SMs) contained in the temporal or temporal-spatial mean coherency matrix $\overline{\boldsymbol{T}}$. The contributions of these different SMs are specified by their corresponding eigenvalues ($\lambda_1$, $\lambda_2$, ($\lambda_3$)) [27], [28].

### C. Coherency Matrix Decomposition Based Polarimetric Persistent Scatterers Interferometry (CMD-PolPSI)

*1) Overall Scheme of CMD-PolPSI:* The principle of the CMD-PolPSI algorithm is to use the eigenvectors of the coherency matrix $\overline{\boldsymbol{T}}$ as different projection vectors to derive interferogram sets, three for the full-pol case and two for the dual-pol. The BEST optimization method [15] is then applied to both the inteferograms derived from the original images, $intfs - Pol$, and those derived from the eigenvector-based projections, $intfs - SM$, to select at pixel level among all interferograms the one with the best phase quality. The scheme of the proposed CMD-PolPSI algorithm is shown in Fig. 1, and it consists of two steps:

*a)* The mean coherency matrix $\overline{\boldsymbol{T}}$ is calculated using (14) and their eigenvectors ($\boldsymbol{u}_1$, $\boldsymbol{u}_2$, ($\boldsymbol{u}_3$)) determined. It has to be noted that for the case of coherence stability $\overline{\gamma}$ based optimization, a spatial multilook, identical to that employed on interferograms generation, has to be applied on $\overline{\boldsymbol{T}}$ before eigenvector-based decomposition. The eigenvectors are used as complex projection vectors $\boldsymbol{\omega}$ to obtain interferogram sets associated with each scattering mechanism ($intfs - SM1, intfs - SM2, (intfs - SM3)$). Depending on the kind of targets, equation (6), for deterministic, or (11), for distributed, is used. These new interferogram sets are referred as $intfs - SM$ in Fig. 1.

*b)* At pixel level, the BEST method [15] is employed to obtain the interferogram set with the best phase quality among the original polarimetric channels, $intfs - Pol$, and the ones derived at the previous step, $intfs - SM$. The final optimized interferogram set, $intfs - CMD$, is then used to estimate ground deformation as classically done with single-pol data.

The phase quality metric used depends on the kind of target considered, the amplitude dispersion $D_A$ in the deterministic case and the mean coherence $\overline{\gamma}$ more suited for the distributed one [16], [21], [24]. Their application is detailed hereafter.

*2) Amplitude Dispersion Optimization:* $D_A$ is calculated differently depending on the origin of the interferogram set. The eigenvector-derived interferograms, $intfs - SM$, use (7)-(8), where the projection vector $\boldsymbol{\omega}$ is replaced by each of the eigenvectors $\boldsymbol{u}_1$, $\boldsymbol{u}_2$, ($\boldsymbol{u}_3$). So, depending on the available
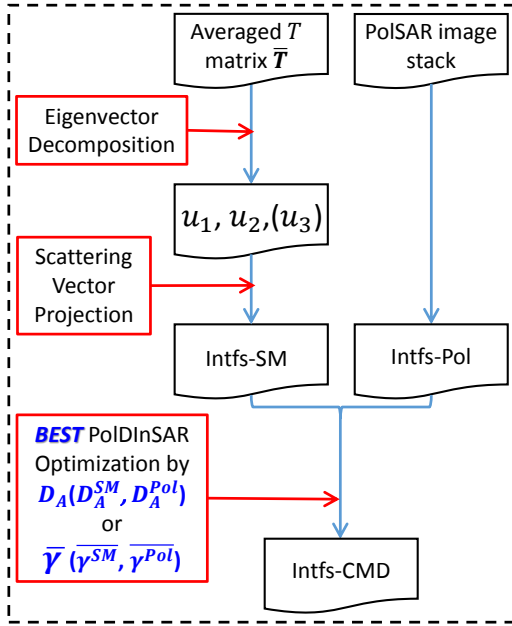
Fig. 1. Diagram of the proposed Coherency Matrix Decomposition based Polarimetric Persistent Scatterers Interferometry (CMD-PolPSI) algorithm.

polarimetric channels three or two values are obtained for each pixel and intereferogram set, $D_A^{SM_1}$, $D_A^{SM_2}$, $(D_A^{SM_3})$. The interferogram sets derived from the original polarimetric channels use the classical expression for $D_A$,

$$D_A^{pol} = \frac{\sigma_A^{pol}}{m_A^{pol}} \qquad (16)$$

where $\sigma_A^{pol}$ and $m_A^{pol}$ are the standard deviation and mean of the amplitudes of the SAR images of the corresponding polarization channel [1].

The BEST optimization method selects among all available interferograms the one with the minimum $D_A$ at pixel level. For the full-pol case six interferogram sets are available,

$$D_A^{min} = min(\underbrace{D_A^{SM_1}, D_A^{SM_2}, D_A^{SM_3}}, \underbrace{D_A^{Pol_1}, D_A^{Pol_2}, D_A^{Pol_3}}) \qquad (17)$$

while for the dual-pol case four interferograms are available,

$$D_A^{min} = min(\underbrace{D_A^{SM_1}, D_A^{SM_2}}, \underbrace{D_A^{Pol_1}, D_A^{Pol_2}}). \qquad (18)$$

*3) Coherence Stability Optimization:* The coherency stability optimization is identical to the one presented with amplitude dispersion. The expressions for calculating the coherence are different depending if it is obtained from the eigenvector-derived interferograms or the original polarization channels ones. For the former, equations (12)-(13) are used, where the projection vector $\omega$ is replaced by $u_1$, $u_2$, $(u_3)$. For the latter, the classical coherence is used,

$$\gamma^{Pol} = \frac{|E[S_1 \cdot S_2^*]|}{\sqrt{E[|S_1|^2] \cdot E[|S_2|^2]}} \qquad (19)$$

where $S_1$ and $S_2$ are the complex pixels of the two SAR images forming the interferogram, $E[]$ and $*$ stand for the

expectation and conjugate operator, respectively. The mean coherence is then obtained as

$$\overline{\gamma^{Pol}} = \frac{1}{N_{intf}} \sum_{k=1}^{N_{intf}} \gamma_k^{Pol} \qquad (20)$$

where $N_{intf}$ is the number of interferograms.

The BEST optimization method selects among all available interferograms the one with maximum $\overline{\gamma}$ at pixel level. For the full-pol case six interferogram sets are available,

$$\overline{\gamma}_{max} = max(\underbrace{\overline{\gamma^{SM_1}}, \overline{\gamma^{SM_2}}, \overline{\gamma^{SM_3}}}, \underbrace{\overline{\gamma^{Pol_1}}, \overline{\gamma^{Pol_2}}, \overline{\gamma^{Pol_3}}}) \qquad (21)$$

while for the dual-pol case only four interferogram sets are available,

$$\overline{\gamma}_{max} = max(\underbrace{\overline{\gamma^{SM_1}}, \overline{\gamma^{SM_2}}}, \underbrace{\overline{\gamma^{Pol_1}}, \overline{\gamma^{Pol_2}}}). \qquad (22)$$

## III. TEST SITES AND DATA SETS

In this paper, three orbital PolSAR data sets with different resolutions and polarimetric channel combinations are used to evaluate the performance of the proposed CMD-PolPSI algorithm.

### A. Full-pol RADARSAT-2 over Barcelona

The Radarsat-2 data set consists of 31 stripmap full-pol images acquired from May 2010 to July 2012 over Barcelona. Radarsat-2 works at C-band and has a revisit period of 24 days. The resolutions of the images are 5.1 m in azimuth and 4.7 m in slant-range. The processing has been applied over an area, covering most of the city and the airport, of 1602 × 4402 pixels.

### B. Dual-pol TerraSAR-X over Murcia

The second data set consists of 31 dual-pol (HH and VV polarizations) images with a temporal span from February 2009 to February 2010, of Murcia city (located in the southeast of Spain). This X-band data has a shorter revisit time of only 11 days. The images' resolution in azimuth and slant-range directions are 2.44 and 0.91 m, respectively. The processed area is 1644 × 2402 pixels covering the central and southern parts of the city.

### C. Dual-pol Sentinel-1B over Mexico City

As a huge amount of dual-pol Sentinel-1 data sets are being freely distributed with a worldwide coverage and short revisit time, PSI applications can be benefited of the polarimetric optimization. Therefore, the proposed CMD-PolPSI is tested on a dual-pol data set over Mexico City, which is one of the most biggest cities in the world suffering from ground deformation [30]–[32]. 30 dual-pol (VV and VH polarizations) images are available, with a time span from May 2017 to May 2018. This C-band sensor has a revisit time of only 12 days. The images' resolutions in azimuth and slant-range directions are 14.0 and 2.3 m, respectively. The processed section is 17089 × 5480 pixels covering most of the city.

## IV. RESULTS

All processing approaches in this paper have been integrated into SUBSIDENCE-GUI, UPC's DInSAR processing chain that implements the Coherent Pixels Technique (CPT) [4], [8]. In this section, the performance of the proposed algorithm is evaluated in terms of phase optimization (through the two phase quality metrics, $D_A$ and mean coherence $\overline{\gamma}$) and final PS pixels' densities of the derived deformation maps. Its performance has been compared with different processing approaches: the single polarization channel (HH or VV), the one using the first eigenvector derived interferogram set $intfs-SM1$ (referred as SM1), the BEST applied to the original polarization channels, the BEST applied to the $intfs-SM$ (referred as SM-BEST) and the ESM optimization method. The comparison of the different approaches will be based on the final number of PS after the PSI processing, not on the original number of PS candidates provided by each method. And some discussions are included regarding the mortality of PS candidates through the PSI processing.

### A. Amplitude Dispersion Based CMD-PolPSI Results

*1) Barcelona Full-pol Radarsat-2 Results:* $D_A$ is a good estimator of phase quality for values below $0.4$ [1]. The smaller the $D_A$, the better the phase quality. Typical thresholds are set to $0.25$ as they lead to a good compromise between phase quality and pixels' density.

$D_A$ histograms obtained with the different approaches are presented in Fig. 2. It can be seen from Fig. 2(a) that all optimization methods improve pixels' phase qualities, w.r.t the HH channel, for $D_A$ below $0.4$. Fig. 2(b) shows a detailed view of the histograms in the pixel selection range, this is $D_A < 0.25$. As expected, ESM is the technique that has the best optimization performance. Except ESM, the proposed CMD-PolPSI achieves the best optimization results, closely followed by SM-BEST and SM1 in the range of pixel selection. SM1 performs a little slightly below SM-BEST, as the two histograms (black and blue lines in Fig. 2(b)) overlap, but much better than BEST. This implies that if there is one dominant scattering mechanism (SM) within one pixel, which is the case for good PSs, it can be well represented by the first eigenvector of its full-pol coherency matrix. For lower quality pixels out of the selection range, the first eigenvalue produces worst results and its performance is even below the single HH channel, as it is shown by Fig. 2(a).

Ground deformation results estimated by the BEST, CMD-PolPSI and ESM approaches are shown in Fig. 3. All methods, using a $D_A$ threshold of 0.25 (around $15°$), have provided similar results in terms of location, magnitude and extend of the different deformation bowls but with different final PS pixel densities, as shown in Table I. Table I presents both the initially selected pixels with the different methods and the final number of pixels, as the PSI processing eliminates some of the originally selected that does not survive the different quality tests. In order to compare the final densities, the results of the HH channel have been used as a reference. Using only the HH channel 78,454 valid pixels have been obtained. BEST is able to rise its number to 164,152, which implies
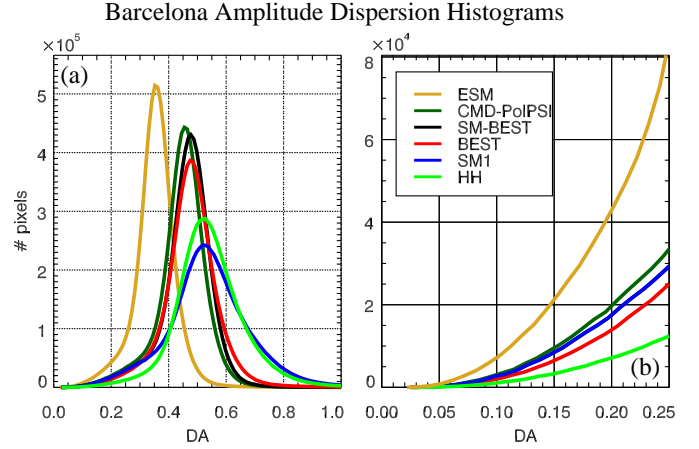


Barcelona Amplitude Dispersion Histograms

Fig. 2. (a) Dispersion of amplitude ($D_A$) histograms using HH polarimetric channel or the SM1, BEST, SM-BEST, ESM and the proposed CMD-PolPSI $D_A$ optimization methods over Barcelona. (b) Detail for $D_A$ values from 0 to 0.25.

an improvement of 109%. CMD-PolPSI achieves 203,030 pixels, an improvement of 159%. Comparing both methods, the proposed CMD-PolPSI is able to retrieve 38,878 additional pixels w.r.t. the BEST method, which accounts for 24% more than BEST. This better performance of CMD-PolPSI is due to the fact that it explores the optimal SM in a more extended space (HH, VV, HV, SM1, SM2 and SM3). As shown in Table II, SM1 represents the 63.5% of the final PS pixels while the other two SM have a marginal contribution. HH and VV channels have similar weights in the obtained pixels, around 10.7%, and HV channel a 15.0%. As expected, the ESM optimization is able to reach the highest density with 499,028 final PS pixels obtained, which represents improvements of 536% w.r.t the HH case and 146% w.r.t the CMD-PolPSI.

*2) Murcia Dual-pol TerraSAR-X Results:* $D_A$ values of HH channel and the five optimization methods over Murcia test site are depicted in Fig. 4. Similar with that of Barcelona area, all polarimetric optimization methods improve pixels' phase qualities, as it is shown in Fig. 4(a). However, the improvement is not as significant as that of the previous full-pol case. This illustrates the limitation of dual-pol data as the search of the optimal channel can only be done in a subspace of that of the full-pol case. Thus, the result is sub-optimal compared with that of the full-pol one.

Fig. 4(b) shows the $D_A$ histograms' details in the pixel selection range, from 0 to 0.25. Differently from the full-pol case, SM-BEST, which performs similarly as BEST, achieves a better phase optimization than the SM1 method. So, the first SM, retrieved by the decomposition of the dual-pol coherency matrix, is not able to well represent the dominant scattering mechanism of the pixel as it was in the full-pol case. For the full-pol case SM1 and SM-BEST produced similar $D_A$ histograms with high quality pixels. CMD-PolPSI produces a higher density of pixels as it is able to combine the best results among HH, VV and SM-BEST. Looking at the percentage of final PS pixels obtained by CMD-PolPSI from each polarimetric channel, summarized in Table II, SM1 represents, as in the full-pol case, the highest percentage, 38.1%, but SM2
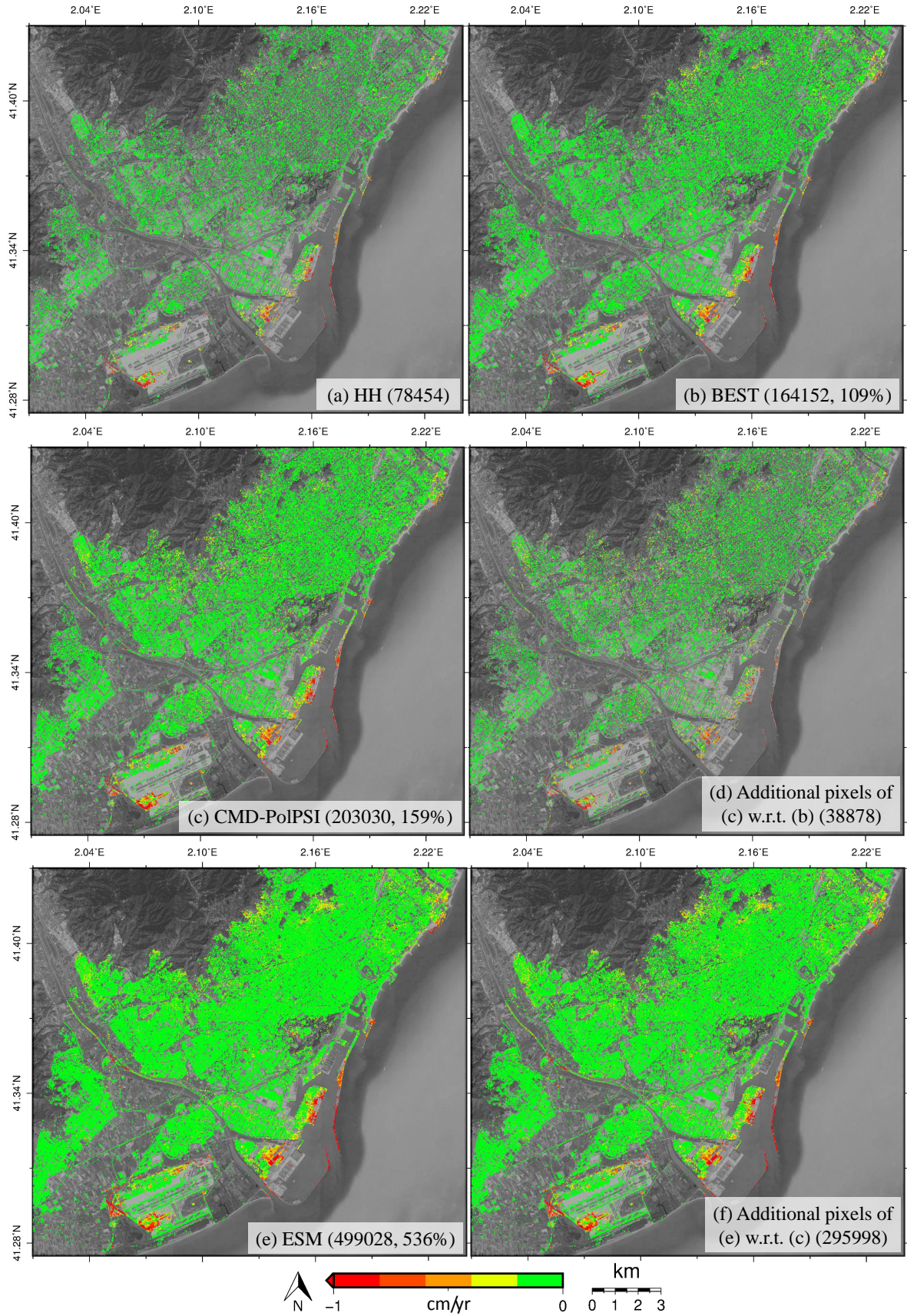
Fig. 3. Ground deformation estimated by (a) HH, (b) BEST, (c) CMD-PolPSI and (e) ESM approaches over **Barcelona**. (d) the additional pixels of CMD-PolPSI w.r.t. BEST, and (f) the additional pixels of ESM w.r.t. CMD-PolPSI. The number in brackets represents the final number of PS pixels for each approach, and the improvement percentage is w.r.t. those derived by the HH approach.

TABLE I
NUMBERS OF PS CANDIDATES AND FINAL PSS OBTAINED BY THE DIFFERENT $D_A$ BASED PSI APPROACHES OVER THE
THREE TEST SITES

| Area App. | Barcelona | Murcia | Mexico City |
|---|---|---|---|
| Single-Pol | 78817(99.5%) / 78454(0%) | 162750(99.8%) / 162513(0%) | 241872(99.8%) / 241415(0%) |
| BEST | 164794(99.6%) / 164152(109%) | 228555(99.8%) / 228211(40%) | 330787(99.8%) / 330263(37%) |
| ESM | 515929(96.7%) / 499028(536%) | 386525(99.7%) / 385407(137%) | 601400(99.7%) /599394(148%) |
| **CMD-PolPSI** | **232083(87.5%) / 203030(159%)** | **268130(98.1%) / 263098(62%)** | **393185(99.8%) / 392585(63%)** |

'App.' is the abbreviation of 'Approach'. "M (i%) / N (j%)" in the table represent the number of PS candidates (M) and the final PS pixels percentage (i%), which equals to $N/M$, the number of final PSs (N) and its corresponding improvement (j%) w.r.t. that of the single polarimetric approach (HH or VV). The Mexico City column gives results of the subarea highlighted by the blue rectangle in Fig. 7(a).

TABLE II
DIFFERENT CHANNELS' CONTRIBUTIONS OF
FINAL PS PIXELS OBTAINED BY $D_A$ BASED
CMD-POLPSI

| Area Ch. | Barcelona | Murcia | Mexico City |
|---|---|---|---|
| HH | 10.7% | 28.8% | — |
| VV | 10.7% | 22.5% | 33.3% |
| HV/VH | 15.0% | — | 16.9% |
| **SM1** | **63.5%** | **38.1%** | **39.3%** |
| SM2 | 0.1% | 10.6% | 10.5% |
| SM3 | 0.0% | — | — |

'Ch.' is the abbreviation of 'Channel', and '—' represents no data.

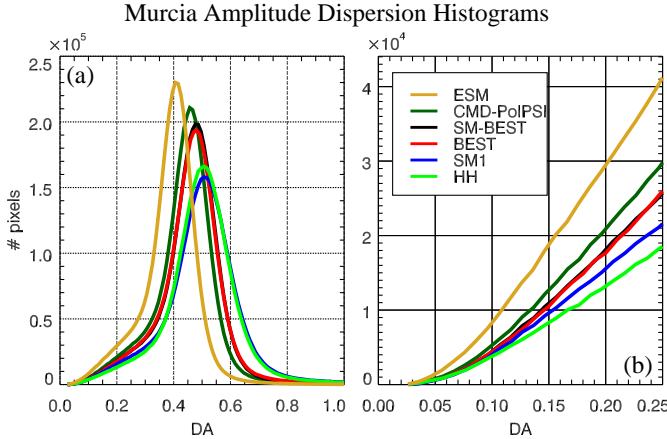represents now the 10.6%. The original channels represent the 28.8% for HH and 22.5% for VV.

Murcia Amplitude Dispersion Histograms



Fig. 4. (a) Dispersion of amplitude ($D_A$) histograms using HH polarimetric channel or the SM1, BEST, SM-BEST, ESM and the proposed CMD-PolPSI optimization methods over Murcia. (b) Detail for $D_A$ values from 0 to 0.25.

The deformation velocity maps estimated by the different approaches are shown by Fig. 5. As Table I shows, final PS pixels obtained by the HH channel, BEST, CMD-PolPSI and ESM are 162,513, 228,211 (40%), 263,098 (62%) and 385,407 (137%), respectively. In brackets it is indicated the percentage of improvement w.r.t the HH case. The final PS pixel density improvements are clearly less significant that the ones obtained in the full-pol case. The influence of the number of polarimetric channels available in the performance of CMD-PolPSI will be further discussed in Section V.

*3) Mexico City Dual-pol Sentinel-1B Results:* The $D_A$ histograms derived from the VV channel and the five approaches over Mexico City are plotted in Fig. 6, which shows very similar trends as that of the previous dual-pol case, Fig. 4. The proposed CMD-PolPSI algorithm is able to work with dual-pol SAR images with lower resolution. Looking at the percentage of final PS pixels from each polarimetric channel, summarized in Table II, the results are very similar to the TerraSAR-X dual-pol case. Once again, SM1 represents the highest percentage, 39.3%, and SM2 the 10.5%. These values are almost identical to the previous case. The original channels represent the 33.3% for VV and 16.9% for VH. The results is not surprising as the cross-pol channel is always weaker than the co-polar ones and thus there are less chances to be selected.

The deformation velocity maps estimated by the dual-pol Sentinel-1B data from May 2017 to May 2018 are shown in Fig. 7. The maximum subsidence velocity reaches up to around 25 cm/yr, and all methods retrieved very similar deformation patterns regardless of their pixel densities. These results are also consistent with the InSAR monitoring results obtained by other authors before 2017 [30]–[32]. The location of the subsidence bowls have not experienced significant changes during the recent years. This rapid ground deformation, which is mainly caused by industrial and agricultural excessive groundwater extraction in this region [30], [33], has not slowed down as our results indicate.

The numbers of final PS pixels achieved by HH, BEST and CMD-PolPSI are 1,263,823, 1,689,300 (34%) and 1,989,047 (57%), respectively. The percentage of improvement in pixels with respect HH channel of the different methods, between brackets, is slightly lower than the one obtained with the TerraSAR-X dual-pol data.

In order to compare their performance with the ESM and avoid an extremely large computational time, the area highlighted by the blue rectangle of Fig. 7(a) has been processed. Fig. 7(c) show the result for the CMD-PolPSI approach that is able to obtain 392,585 final PS pixels, a 63% of increase w.r.t. the VV channel. As expected, ESM produces the highest density of pixels, a total of 599,394 that represents a 148% of increase w.r.t. the VV channel, as it is shown in Table I.

*4) PS candidates mortality through the PSI processing:* Not all initially selected pixels, the PS candidates, survive the PSI processing. During it, different quality tests are implemented to eliminate those pixels that does not pass a threshold
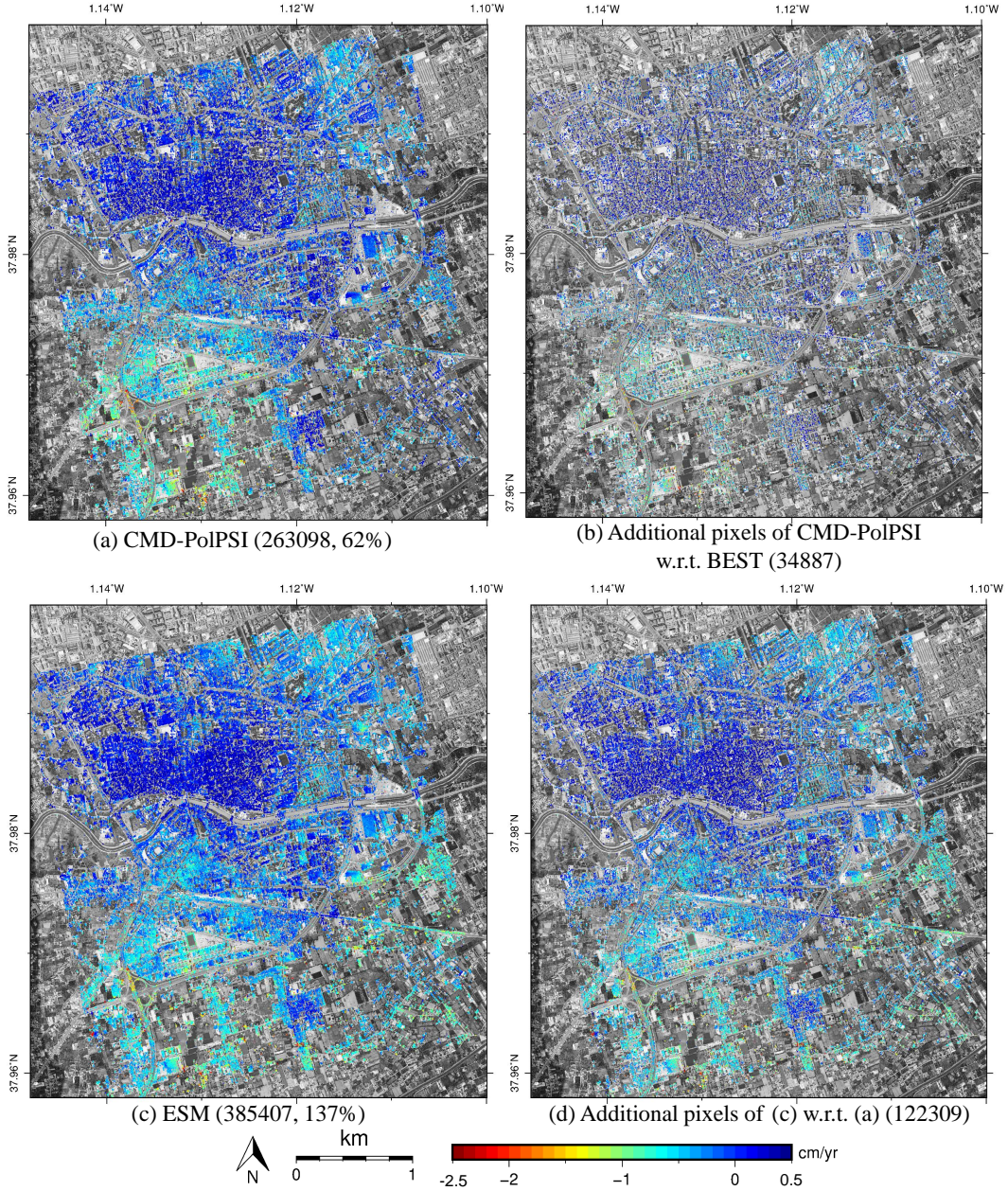
Fig. 5. **Murcia** deformation velocity maps derived by (a) the proposed CMD-PolPSI approaches, and (c) the ESM method. (b) is the additional pixels of CMD-PolPSI w.r.t. the BEST approach, and (d) is the additional pixels of (c) w.r.t. (a). The number in the bracket represents the number of final PS pixels obtained by each approach, and the improvement percentage is w.r.t. those derived by the HH approach.

(like model adjustment and integration consistency). So, it is interesting to compare the mortality of the PS candidates through the PSI processing for all methods. From the presented results summarized in Table I, the highest mortality is for the full-pol data. Single-pol and BEST methods losses less than 1% of PS candidates during the PSI processing, while ESM and CMD-PolPSI around 10% and 4%, respectively. It seems that the optimization is able to create some solutions that are not consistent and being just mathematical artifacts. On the contrary, for dual-pol data rejection rates are below 2% for all cases.

### B. Coherence Stability Based CMD-PolPSI Results

*1) Coherence Optimization Results:* The coherence-based phase optimization approaches requires a multilook of interferograms. The down-sampling average method has been used, and images' resolution has been reduced. The averaging window sizes (azimuth × range) for Radarsat-2, TerraSAR-X and Sentinel-1B SAR data are $5 \times 3$, $3 \times 6$ and $3 \times 18$, respectively. It is worth to be mentioned that the sizes of these three averaging windows are identical to those that respectively applied on $\overline{T}$ of the three datasets before the eigenvector-based decomposition.

The mean coherence histograms of the single-pol data set and the optimized ones over the three test sites are shown
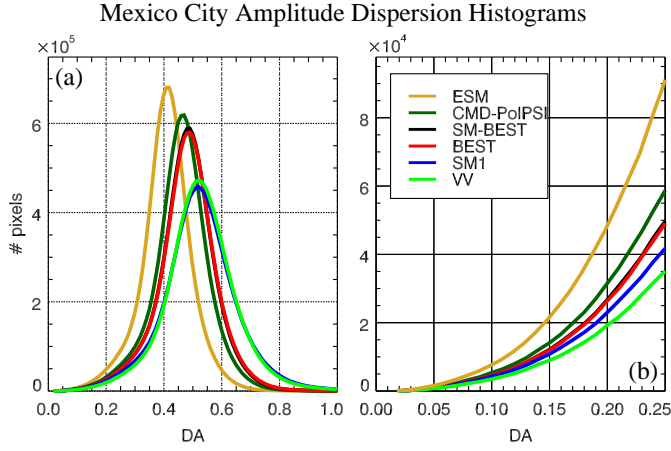
Fig. 6. (a) Dispersion of amplitude ($D_A$) histograms using VV polarimetric channel or the SM1, BEST, SM-BEST, ESM and the proposed CMD-PolPSI $D_A$ optimization methods over **Mexico City**. (b) Detail for $D_A$ values from 0 to 0.25.

in Fig. 8. It can be seen from them that, excluding the ESM method, the proposed CMD-PolPSI algorithm presents the best phase optimization effect over all the three sites. However, the improvement, w.r.t. the single-pol channel, achieved by the coherence stability based CMD-PolPSI is not as significant as that of $D_A$ based CMD-PolPSI. This can also be applied to the other optimization methods (SM1, BEST and SM-Best). The main reason for this reduction is the degradation of pixels' resolutions due to the multilook that mixes the different scattering mechanisms present in the averaged pixels. This makes it harder to find a dominant scattering mechanism at the pixel's optimization step.

Among the scenarios, the optimization improvement of the full-pol Radarsat-2 (Fig. 8(b)) and dual-pol TerraSAR-X (Fig. 8(d)) data sets are much better than that of the dual-pol Sentinel-1B data set, as Fig. 8(f) shows. Two conditionings are overlapped. Firstly, the larger the number of polarimetric channels the better the optimization techniques perform. Full-pol data always outperforms dual-pol one as more independent measurements are available. Secondly, the finer the resolution the better the optimization techniques perform as the chances of having a distinctive scattering mechanism in a pixel are higher. This point is linked to the multilook applied to the interferograms. This effect is clearly seen in the difference in performance between TerraSAR-X, good resolution and moderate multilook, and Sentinel data, worst resolution and higher multilook.

*2) Pixel Selection Results:* If the phase standard deviation (STD) threshold for pixel selection is set around $15°$, same as that of $D_A$ based optimization, the threshold on $\overline{\gamma}$ can be set from the relationship between the estimated coherence $\overline{\gamma}$ and its phase STD [34]. Due to the usual oversampling of SAR images, the number of independent pixels in multilook processing averaged when computing the multilooked interferograms, also known as Equivalent Number of Looks, is smaller than the number of averaged samples. This fact has been accounted for when determining the three thresholds [29]. Thus, the $\overline{\gamma}$ thresholds for each case have been set to 0.55 (Barcelona),

0.72 (Murcia) and 0.40 (Mexico City). The results regarding the number of pixels selected (i.e. PS candidates) and final PSs in each scenario, the optimization method and coherence thresholds are summarized in Table III.

Since the multilook has reduced the number of pixels, the performance of the coherence approach can not be directly compared with the previous full-resolution $D_A$ case. Instead of the number of pixels selected, the pixels' increase w.r.t. the single-pol approach is used. With the quad-pol data over Barcelona, coherence threshold set as 0.55, the final PS pixels' improvements by the three approaches (BEST, CMD-PolPSI and ESM) w.r.t. the single-pol approach are 33%, 40% and 58%, respectively. These improvements are smaller than their counterparts of the $D_A$ based methods, which were 109%, 159% and 536%, respectively. For Murcia and Mexico City dual-pol cases, the increase in final PS pixel densities is being further reduced. This is is mainly due to the reduced number of polarimetric channels, pixels' resolutions and applied multilook. With the Sentinel-1 data, to which a higher multilook has been applied, the increase in pixels is marginal for all optimization methods when 0.4 is set as the selection threshold. Table III also shows an interesting point. If the selection threshold is being more restrictive, with values tending to 1, to select only the highest quality pixels, the improvement in final PS pixels density thanks to the polarimetric optimization increases. The highest quality pixels can be associated with those in which there is a significant scatterer that can also be associated with a distinctive and isolated scattering mechanism, which justifies the better performance of the polarimetric optimization.

## V. DISCUSSION

### A. Comparison of Dual-pol and Full-pol Data Sets Based CMD-PolPSI

The presented results have clearly shown that full-pol data always outperforms dual-pol one when applying polarimetric optimization techniques. However, as the three data sets belong to different sensors (with different wavelengths, resolutions and polarimetric channels) and scenarios it is only possible to extract qualitative conclusions. Thus, to better investigate the impact of the number and type of polarimetric channels on CMD-PolPSI's performance over the same scenario and sensor, the Radarsat-2 quad-pol data has been used to generate three different dual-pol data sets: HH+VV, HH+HV and VV+HV.

After processing the four data sets, Fig. 9 represents the histograms of the ratio between pixels detected for each dual-pol case (HH+VV, HH+HV and VV+HV) divided by the ones selected with the full-pol data (HH+VV+HV). The red line, i.e. ratio equals to one, is plotted as a reference. As Fig. 9(a) shows, the three dual-pol combinations present similar results with ratios below one for $D_A$ values below 0.45, which means there are more high quality pixels after optimization by using the full-pol data than with any of the dual-pol ones. Fig. 9(b) shows that among the dual-pol case the HH+VV combination presents the best phase optimization. More concretely, if 0.25 is set as the $D_A$ threshold, the pixels selected from the full-pol, HH+VV, HH+HV and VV+HV data sets are 240,268

(a) CMD-PolPSI (1989047, 57%)

(b) Additional pixels of CMD-PolPSI w.r.t. BEST (299717)

(c) CMD-PolPSI of subsection (392585, 63%)

(d) ESM of subsection (599394, 148%)

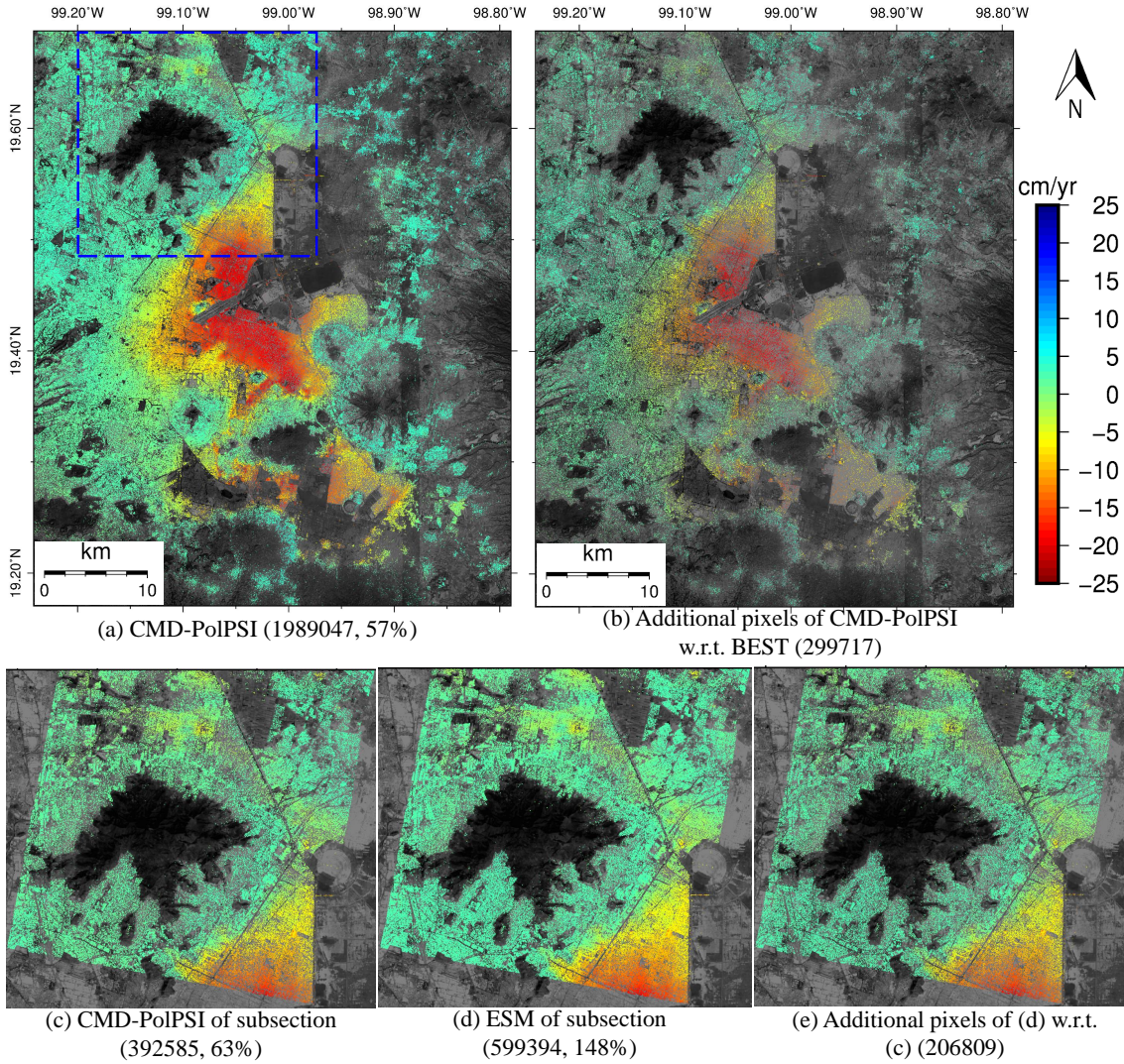(e) Additional pixels of (d) w.r.t. (c) (206809)

Fig. 7. **Mexico City** deformation velocity map derived by (a) CMD-PolPSI, and (b) the additional pixels of CMD-PolPSI w.r.t. the BEST approach. (c) and (d) the results retrieved by CMD-PolPSI and ESM of the subsection, highlighted by the blue dashed rectangle in (a). (e) the additional pixels of ESM w.r.t. CMD-PolPSI in the subsection. The number in the bracket represents the number of final PS pixels obtained by each approach. The percentage is the increase w.r.t. the final PS pixels obtained from the VV channel.

(100%), 160,540 (66.8%), 157,675 (65.6%), 152,882 (63.6%), respectively. In average, the final number of selected pixels with dual-pol data is reduced around the 33% with respect to the full-pol case. This degradation on the optimization performance is due to the lack of cross-polar or co-polar information in the coherency matrix, which can lead to the failure of correctly extracting pixels' dominant SMs [35], [36]. The ESM method presents the same behavior.

## B. Comparison with the ESM Algorithm

The ESM algorithm exploits the optimal projection vector through the full solution space, thus it presents much better phase optimization effects than the other methods. The results over the three test-sites have proved this point. However, the computational burden of ESM is much higher than that of CMD-PolPSI, which can make it extremely costly to apply for large scenes. Particularly, for the Barcelona full-pol data set (1602 × 4402 pixels), ESM takes 271,900 seconds (around

75.5 hours) for the $D_A$ based phase optimization and the CMD-PolPSI just 1,068 seconds (around 0.3 hours), which is 255 times faster than ESM. For the Murcia dual-pol TerraSAR-X case (1644 × 2402) the processing time are 435 seconds (around 0.12 hour) and 15,205 (around 4.2 hour) seconds for CMD-PolPSI and ESM, respectively. For large areas, especially for full-pol data sets, the computational burden of ESM can limit its application. For instance, if applied on the Mexico city data set (17089 × 5480 pixels), assuming that optimization time for each pixel is the same as that of Barcelona case, 1002.6 hours (around 42 days) would be required for the polarimetric optimization step. If CMD-PolPSI is employed, the processing time is reduced to around 4 hours. These tests indicate that the proposed CMD-PolPSI is much more computationally efficient than ESM but with the price of a lower performance in terms of phase optimization. The above experiments have been carried out on a workstation equipped with an 8-core Intel(R) Xeon(R) E5620 processor (2.4 GHz)

TABLE III
PIXELS SELECTED WITH DIFFERENT MEAN COHERENCE THRESHOLDS USING DIFFERENT PHASE OPTIMIZATION APPROACHES OVER THE THREE TEST SITES

| App. $\overline{\gamma}$ | Single-pol | BEST | ESM | **CMD-PolPSI** |
|---|---|---|---|---|
| **Barcelona** | | | | |
| $\geq$**0.55** | 92340(99.7%) / 92045(0%) | 123342(99.6%) / 122866(33%) | 146427(99.5%) / 145649(58%) | **129777(99.5%) / 129208(40%)** |
| $\geq$0.7 | 45913(99.7%) / 45784(0%) | 73818(99.7%) / 73621(61%) | 100678(99.7%) / 100364(119%) | **83490(99.7%) / 83240(82%)** |
| $\geq$0.9 | 5976(99.7%) / 5960(0%) | 10609(99.7%) / 10581(78%) | 18176(99.7%) / 18127(204%) | **14259(99.7%) / 14223(139%)** |
| **Murcia** | | | | |
| $\geq$**0.72** | 51523(99.8%) / 51412(0%) | 62067(99.8%) / 61940(20%) | 74748(99.7%) / 74508(45%) | **67947(99.7%) / 67754(32%)** |
| $\geq$0.8 | 33553(99.8%) / 33489(0%) | 41435(99.8%) / 41354(23%) | 53716(99.7%) / 53578(60%) | **47457(99.8%) / 47347(41%)** |
| $\geq$0.9 | 12459(99.9%) / 12447(0%) | 15626(99.9%) / 15608(25%) | 23482(99.9%) / 23450(88%) | **19841(99.9%) / 19814(59%)** |
| **Mexico City** | | | | |
| $\geq$**0.4** | 116814(99.8%) / 116623(0%) | 119507(99.8%) / 119304(2%) | 122953(99.8%) / 122715(5%) | **120561(99.8%) / 120355(3%)** |
| $\geq$0.7 | 34658(99.9%) / 34612(0%) | 38797(99.9%) / 38752(12%) | 45310(99.9%) / 45255(31%) | **41386(99.9%) / 41335(19%)** |
| $\geq$0.9 | 2622(96.4%) / 2527(0%) | 3066(96.8%) / 2967(17%) | 3627(97.0%) / 3521(39%) | **3320(96.9%) / 3218(27%)** |

'App.' is the abbreviation of 'Approach'. "M (i%) / N (j%)" in the table represent the number of PS candidates (M) and the percentage of final PS pixels (i%), which equals to $N/M$, the final number of PSs (N) and its increase (j%) w.r.t. that of the single polarimetric approach (HH or VV). The Mexico City column gives results of the subarea highlighted by the blue rectangle in Fig. 7(a).

and 60 GB of RAM. The implementation of the software is in IDL.

### C. Possible Variations of the Proposed CMD-PolPSI

In this paper, for the sake of simplicity and efficiency, the eigenvector-based decomposition is used to decompose the coherency matrix in the CMD-PolPSI algorithm. It is worth to be noted that other PolSAR decomposition methods, like the classical Huynen and Cloude decomposition [28] or the advanced Yamaguchi decomposition [37]–[39], can also be employed for the coherency matrix decomposition. By replacing the eigenvector-based decomposition with other Pol-SAR decomposition methods, other variations of the proposed CMD-PolPSI can be easily built.

## VI. CONCLUSION

In this paper, a new Polarimetric Persistent Scatterers Interferometry (PolPSI) algorithm based on the coherency matrix decomposition has been proposed. This PolPSI algorithm, referred as CMD-PolPSI, produces optimization results better than the simple BEST approach. On the other side, the ESM methods outperforms CMD-PolPSI but its high computational burden reduces its applicability to large areas. CMD-PolPSI, thus, constitutes a good compromise between pixel density improvement and computational burden. Two approaches have been developed, one oriented to permanent scatters (PS) that uses the dispersion of amplitude $D_A$ as pixel selection criteria, and the other better for distributed scatterers (DS) based on the mean coherence from multilooked interferograms.

Three complementary data sets in terms of polarization (Radarsat-2 full-pol, TerraSAR-X and Sentinel-1 dual-pol), wavelength (C and X-band) and image resolution have been used to evaluate the performance of the proposed algorithm in different conditions. In terms of interferometric phase optimization, CMD-PolPSI presents better performance than BEST in all three data sets and, as expected, below ESM. The best results are always achieved with full-pol data at the highest resolution.

With the $D_A$ approach, for full-pol data the improvement obtained by CMD-PolPSI in final PS pixels' density has been 159% w.r.t. the single-pol HH processing while BEST has been able to improve only by a 109%. The dual-pol datasets have produced lower improvements, for TerraSAR-X data a 62%, compared with the 40% of BEST, and for Sentinel-1 a 63%, while BEST has been a 37%. For all three cases, ESM has been able to produce improvements of 536%, 137% and 148% respectively. The full-pol dataset has been used to generate all possible dual-pol combinations in order to evaluate, under exactly the same conditions, which one performs better. Among them, HH+VV data is the one that produces the highest improvement in number of selected pixels.

The coherence approach with multilooked interferograms has produced lower improvements and, as a general rule, the lower the interferograms resolution (as a combination of the original image resolution and applied multilook) the worst the polarimetric optimization performs. Using the same phase quality threshold as with the $D_A$ approach, the improvements achieved by CMD-PolPSI on numbers of final PS pixels are limited to 40%, 32% and 3% w.r.t the single-pol case for Radarsat-2, TerraSAR-X and Sentinel-1, respectively. It is worth to note that if the selection threshold is more restrictive, this is higher coherence values, the improvements increase as well. For instance, coherencies above 0.9 produce improvements of 139%, 59% and 27% by CMD-PolPSI w.r.t. single-pol case, respectively. In this case, with the highest coherence thresholds, pixels with a single and significant scattering mechanism are being selected.

Compared with the powerful ESM algorithm, the proposed CMD-PolPSI has a lower computational burden, being around 255 times faster with full-pol data for the $D_A$ based optimization (full resolution optimization). On the other hand, ESM presents much better optimization results as it is able to explore the full space of polarimetric scattering mechanisms. In practice, CMD-PolPSI is able to provide a good compromise between computational burden and pixels' density improvement when performing PSI processing in cases that
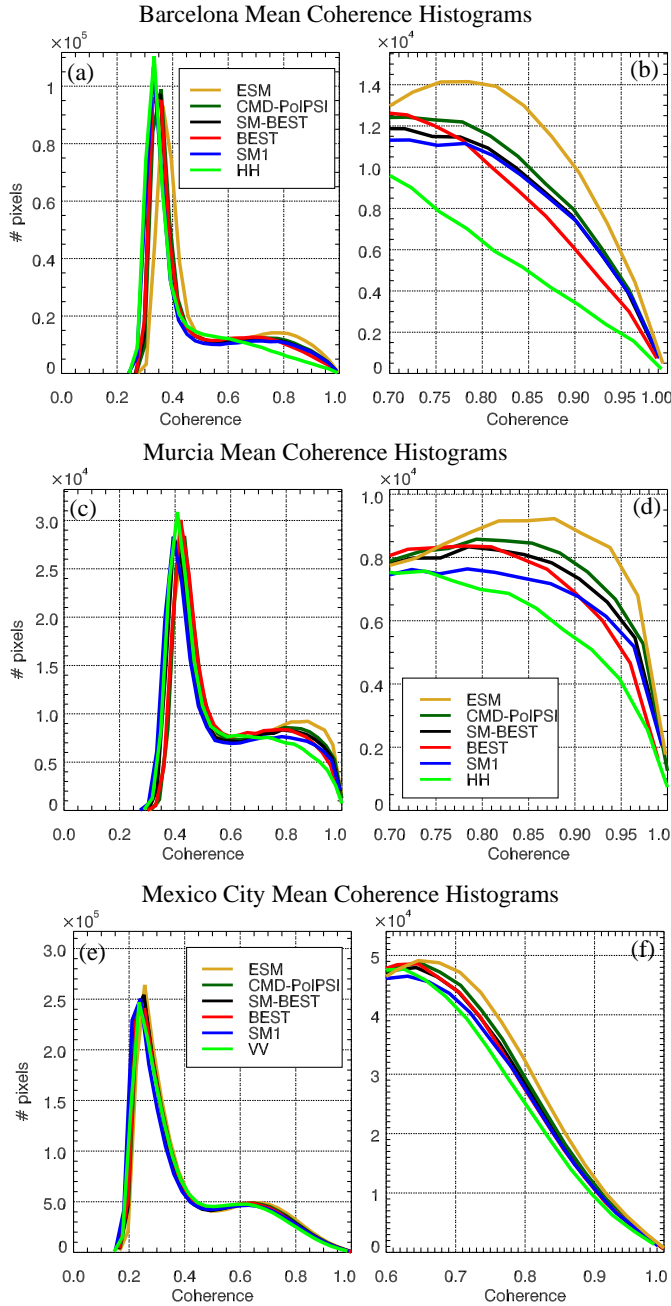
## Barcelona Mean Coherence Histograms



## Murcia Mean Coherence Histograms



## Mexico City Mean Coherence Histograms



Fig. 8. Mean coherence ($\overline{\gamma}$) histograms using single polarimetric channel (HH/VV) or the SM1, BEST, SM-BEST, ESM and the proposed CMD-PolPSI optimization methods over the three test sites ((a), (c), (e)), and corresponding details of $\overline{\gamma}$ with larger values ((b), (d), (f)).
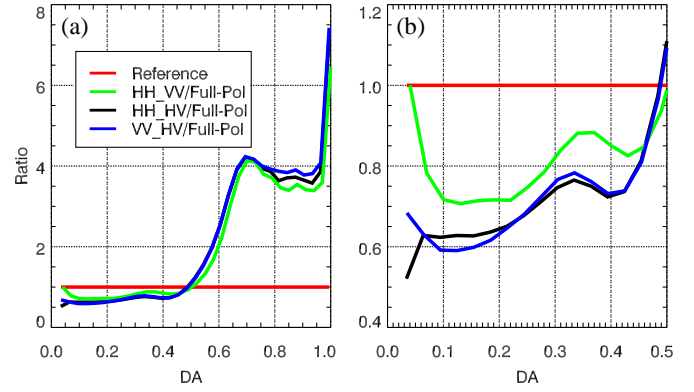
wide areas have to be processed.

Fig. 9. (a) Ratios between the dual-pol and full-pol data sets derived $D_A$ histograms over Barcelona test site by using the CMD-PolPSI algorithm. (b) Detail of (a) in the $D_A$ range from 0 to 0.5.

## REFERENCES

[1] A. Ferretti, C. Prati, and F. Rocca, "Permanent scatterers in SAR interferometry," *IEEE Transactions on geoscience and remote sensing*, vol. 39, no. 1, pp. 8–20, 2001.

[2] ——, "Nonlinear subsidence rate estimation using permanent scatterers in differential SAR interferometry," *IEEE Transactions on geoscience and remote sensing*, vol. 38, no. 5, pp. 2202–2212, 2000.

[3] P. Berardino, G. Fornaro, R. Lanari, and E. Sansosti, "A new algorithm for surface deformation monitoring based on small baseline differential SAR interferograms," *IEEE Transactions on Geoscience and Remote Sensing*, vol. 40, no. 11, pp. 2375–2383, 2002.

[4] O. Mora, J. J. Mallorqui, and A. Broquetas, "Linear and nonlinear terrain deformation maps from a reduced set of interferometric SAR images," *IEEE Transactions on Geoscience and Remote Sensing*, vol. 41, no. 10, pp. 2243–2253, 2003.

[5] R. Lanari, O. Mora, M. Manunta, J. J. Mallorquí, P. Berardino, and E. Sansosti, "A small-baseline approach for investigating deformations on full-resolution differential SAR interferograms," *IEEE Transactions on Geoscience and Remote Sensing*, vol. 42, no. 7, pp. 1377–1386, 2004.

[6] A. Hooper, H. Zebker, P. Segall, and B. Kampes, "A new method for measuring deformation on volcanoes and other natural terrains using InSAR persistent scatterers," *Geophysical research letters*, vol. 31, no. 23, 2004.

[7] A. Hooper, P. Segall, and H. Zebker, "Persistent scatterer interferometric synthetic aperture radar for crustal deformation analysis, with application to volcán alcedo, galápagos," *Journal of Geophysical Research: Solid Earth*, vol. 112, no. B7, 2007.

[8] P. Blanco-Sanchez, J. J. Mallorquí, S. Duque, and D. Monells, "The coherent pixels technique (CPT): An advanced DInSAR technique for nonlinear deformation monitoring," *Pure and Applied Geophysics*, vol. 165, no. 6, pp. 1167–1193, 2008.

[9] R. Iglesias, J. J. Mallorqui, and P. López-Dekker, "DInSAR pixel selection based on sublook spectral correlation along time." *IEEE Trans. Geoscience and Remote Sensing*, vol. 52, no. 7, pp. 3788–3799, 2014.

[10] G. Savio, A. Ferretti, F. Novali, S. Musazzi, C. Prati, and F. Rocca, "PSInSAR validation by means of a blind experiment using dihedral reflectors," in *FRINGE 2005 workshop*, vol. 610, 2006.

[11] F. Casu, M. Manzo, and R. Lanari, "A quantitative assessment of the SBAS algorithm performance for surface deformation retrieval from DInSAR data," *Remote Sensing of Environment*, vol. 102, no. 3-4, pp. 195–210, 2006.

[12] F. Zhao and J. J. Mallorqui, "A temporal phase coherence estimation algorithm and its application on DInSAR pixel selection," *IEEE Transactions on Geoscience and Remote Sensing, Undergoing Review*.

[13] A. Ferretti, A. Fumagalli, F. Novali, C. Prati, F. Rocca, and A. Rucci, "A new algorithm for processing interferometric data-stacks: SqueeSAR," *IEEE Transactions on Geoscience and Remote Sensing*, vol. 49, no. 9, pp. 3460–3470, 2011.

[14] G. Fornaro, S. Verde, D. Reale, and A. Pauciullo, "CAESAR: An approach based on covariance matrix decomposition to improve multibaseline–multitemporal interferometric SAR processing," *IEEE Transactions on Geoscience and Remote Sensing*, vol. 53, no. 4, pp. 2050–2065, 2015.

[15] L. Pipia, X. Fabregas, A. Aguasca, C. Lopez-Martinez, S. Duque, J. J. Mallorqui, and J. Marturia, "Polarimetric differential SAR interferometry: First results with ground-based measurements," *IEEE Geoscience and Remote Sensing Letters*, vol. 6, no. 1, pp. 167–171, 2009.

[16] V. D. Navarro-Sanchez, J. M. Lopez-Sanchez, and F. Vicente-Guijalba, "A contribution of polarimetry to satellite differential SAR interferometry: Increasing the number of pixel candidates," *IEEE Geoscience and Remote Sensing Letters*, vol. 7, no. 2, pp. 276–280, 2010.

[17] D. Monells, R. Iglesias, J. J. Mallorquí, X. Fàbregas, and C. Lopez-Martinez, "Phase quality optimization in orbital differential SAR interferometry with fully polarimetric data," in *Geoscience and Remote Sensing Symposium (IGARSS), 2012 IEEE International*. IEEE, 2012, pp. 1864–1867.

[18] R. Iglesias, X. Fabregas, A. Aguasca, C. López-Martínez, and A. Alonso-González, "Advanced polarimetric optimization for DInSAR applications with ground-based SAR," in *Synthetic Aperture Radar, 2012. EUSAR. 9th European Conference on*. VDE, 2012, pp. 513–516.

[19] V. D. Navarro-Sanchez and J. M. Lopez-Sanchez, "Improvement of persistent-scatterer interferometry performance by means of a polarimetric optimization," *IEEE Geoscience and Remote Sensing Letters*, vol. 9, no. 4, pp. 609–613, 2012.

[20] R. Iglesias, D. Monells, X. Fabregas, J. J. Mallorqui, A. Aguasca, and C. Lopez-Martínez, "Phase quality optimization techniques and limitations in polarimetric differential SAR interferometry," *transformation*, vol. 17, p. 18, 2013.

[21] R. Iglesias, D. Monells, X. Fabregas, J. J. Mallorqui, A. Aguasca, and C. Lopez-Martinez, "Phase quality optimization in polarimetric differential SAR interferometry," *IEEE transactions on geoscience and remote sensing*, vol. 52, no. 5, pp. 2875–2888, 2014.

[22] R. Iglesias, D. Monells, C. López-Martínez, J. J. Mallorqui, X. Fabregas, and A. Aguasca, "Polarimetric optimization of temporal sublook coherence for DInSAR applications," *IEEE Geoscience and Remote Sensing Letters*, vol. 12, no. 1, pp. 87–91, 2015.

[23] Z. Sadeghi, M. J. V. Zoej, A. Hooper, and J. M. Lopez-Sanchez, "A new polarimetric persistent scatterer interferometry method using temporal coherence optimization," *IEEE Transactions on Geoscience and Remote Sensing*, no. 99, pp. 1–9, 2018.

[24] V. D. Navarro-Sanchez and J. M. Lopez-Sanchez, "Spatial adaptive speckle filtering driven by temporal polarimetric statistics and its application to PSI," *IEEE Transactions on Geoscience and Remote Sensing*, vol. 52, no. 8, pp. 4548–4557, 2014.

[25] B. Wu, L. Tong, Y. Chen, and L. He, "New methods in multibaseline polarimetric SAR interferometry coherence optimization," *IEEE Geoscience and Remote Sensing Letters*, vol. 12, no. 10, pp. 2016–2020, 2015.

[26] ——, "Improved SNR optimum method in PolDInSAR coherence optimization," *IEEE Geoscience and Remote Sensing Letters*, vol. 13, no. 7, pp. 982–986, 2016.

[27] S. R. Cloude and K. P. Papathanassiou, "Polarimetric SAR interferometry," *IEEE Transactions on Geoscience and Remote Sensing*, vol. 36, no. 5, pp. 1551–1565, 1998.

[28] J.-S. Lee and E. Pottier, *Polarimetric radar imaging: from basics to applications*. CRC press, 2009.

[29] V. D. Navarro-Sanchez, J. M. Lopez-Sanchez, and L. Ferro-Famil, "Polarimetric approaches for persistent scatterers interferometry," *IEEE Transactions on Geoscience and Remote Sensing*, vol. 52, no. 3, pp. 1667–1676, 2014.

[30] X. Wang, Q. Zhang, C. Zhao, F. Qu, and J. Zhang, "A novel method of generating deformation time-series using interferometric synthetic aperture radar and its application in Mexico City," *Remote Sensing*, vol. 10, no. 11, p. 1741, 2018.

[31] S. V. Samsonov and N. d'Oreye, "Multidimensional small baseline subset (MSBAS) for two-dimensional deformation analysis: Case study Mexico City," *Canadian Journal of Remote Sensing*, vol. 43, no. 4, pp. 318–329, 2017.

[32] A. Sowter, M. B. C. Amat, F. Cigna, S. Marsh, A. Athab, and L. Alshammari, "Mexico City land subsidence in 2014–2015 with Sentinel-1 IW TOPS: Results using the intermittent SBAS (ISBAS) technique," *International Journal of Applied Earth Observation and Geoinformation*, vol. 52, pp. 230–242, 2016.

[33] J. Carrera-Hernández and S. Gaskin, "The basin of Mexico aquifer system: regional groundwater level dynamics and database development," *Hydrogeology Journal*, vol. 15, no. 8, pp. 1577–1590, 2007.

[34] R. F. Hanssen, *Radar interferometry: data interpretation and error analysis*. Springer Science & Business Media, 2001, vol. 2.

[35] S. Cloude, "The dual polarization entropy/alpha decomposition: A PALSAR case study," in *Science and Applications of SAR Polarimetry and Polarimetric Interferometry*, vol. 644, 2007.

[36] K. Ji and Y. Wu, "Scattering mechanism extraction by a modified Cloude-Pottier decomposition for dual polarization SAR," *Remote Sensing*, vol. 7, no. 6, pp. 7447–7470, 2015.

[37] Y. Yamaguchi, T. Moriyama, M. Ishido, and H. Yamada, "Four-component scattering model for polarimetric SAR image decomposition," *IEEE Transactions on Geoscience and Remote Sensing*, vol. 43, no. 8, pp. 1699–1706, 2005.

[38] Y. Yamaguchi, Y. Yajima, and H. Yamada, "A four-component decomposition of polsar images based on the coherency matrix," *IEEE Geoscience and Remote Sensing Letters*, vol. 3, no. 3, pp. 292–296, 2006.

[39] Y. Yamaguchi, A. Sato, W.-M. Boerner, R. Sato, and H. Yamada, "Four-component scattering power decomposition with rotation of coherency matrix," *IEEE Transactions on Geoscience and Remote Sensing*, vol. 49, no. 6, pp. 2251–2258, 2011.
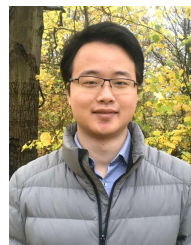
**Feng Zhao** (S'17) received the M.S. degrees in geodesy and surveying engineering from China University of Mining and Technology, Xuzhou, China, in 2016. He is currently working toward the Ph.D. degree at the Universitat Politècnica de Catalunya, Barcelona, Spain.

He joined the CommSensLab, Universitat Politècnica de Catalunya, in September 2016, where his main work focuses on the development of advanced pixel selection and optimization algorithms for multi-temporal (Pol)DInSAR techniques. His research interests include advanced multi-temporal InSAR techniques and its application on terrain deformation detection.

**Jordi J. Mallorqui** (S'93-M'96-SM'13) was born in Tarragona, Spain, in 1966. He received the Ingeniero degree in telecommunications engineering and the Doctor Ingeniero degree in telecommunications engineering for his research on microwave tomography for biomedical applications in the Department of Signal Theory and Communications from the Universitat Polit'ecnica de Catalunya (UPC), Barcelona, Spain, in 1990 and 1995, respectively. Since 1993, he has been teaching at the School of Telecommunications Engineering of Barcelona, UPC, first as an Assistant Professor, later in 1997 as an Associate Professor, and since 2011 as a Full Professor. Since October 2017 he is the Director of the Department of Signal Theory and Communications (UPC).

His teaching activity involves microwaves, radionavigation systems, and remote sensing. He spent a sabbatical year with the Jet Propulsion Laboratory, Pasadena, CA, USA, in 1999, working on interferometric airborne synthetic aperture radar (SAR) calibration algorithms. He is currently working on the application of SAR interferometry to terrain deformation monitoring with orbital, airborne, and ground data; vessel detection and classification from SAR images; and 3-D electromagnetic (EM) simulation of SAR systems. He is also collaborating in the design and construction of a ground-based SAR interferometer for landslide control. He has published more than 100 papers on microwave tomography, EM numerical simulation, SAR processing, interferometry, and differential interferometry in refereed journals and international symposia.